




Cite this: DOI: 10.1039/d5ew00485c

## Towards sustainable PMR for organic contaminant removal from municipal wastewater

Veronica Cozzolino,<sup>ab</sup> Gerardo Coppola,<sup>b</sup> Sudip Chakraborty,<sup>b</sup>  
 Giovanni Chiappetta,<sup>a</sup> Alessio Siciliano,<sup>c</sup> Carlo Limonti,<sup>c</sup> Giulia Maria Curcio,<sup>c</sup>  
 Catia Algieri <sup>\*a</sup> and Vincenza Calabrò<sup>b</sup>

Persistent organic pollutants (POPs) are dangerous for the human body and for the environment, due to their high chemical stability at low concentrations and low biodegradability. Traditional treatment plants are inadequate or inefficient, making their removal from water very difficult. Unlike most existing studies that rely on synthetic wastewater, the novelty of this work lies in studying the photocatalytic degradation of POPs in real urban wastewater using titanium dioxide-based slurry reactors. A distinctive contribution of this work also lies in the comparison of two reactor configurations (internal vs. external UV sources), supported by finite element modelling (FEM) to simulate and optimize light distribution. The results showed that the configuration with an immersed lamp, which ensures better light distribution, leads to enhanced catalytic activity at lower photocatalyst concentration and low light power. This optimal configuration was subsequently applied in a slurry photocatalytic membrane reactor (SPMR), resulting in improved pollutant removal efficiency. In particular, experimental results demonstrated that using an inorganic membrane with a molecular weight cut-off of 1 kDa achieved approximately a 15% increase in pollutant removal efficiency. This integrated, experimentally validated approach addresses a critical gap in translating lab-scale photocatalysis research to real wastewater treatment.

Received 28th May 2025,  
 Accepted 29th July 2025

DOI: 10.1039/d5ew00485c

rsc.li/es-water

### Water impact

This work is focused on the development of a slurry photocatalytic membrane reactor (SPMR) for the removal of recalcitrant pollutants from municipal wastewater. In particular, the photodegradation of persistent pollutants in real urban wastewater was initially evaluated using a TiO<sub>2</sub>-photocatalytic batch reactor. Two reactor configurations were considered: one with a flat UV lamp and another with submerged UV lamps. The photoreactor equipped with submerged lamps demonstrated superior performance in terms of COD (chemical oxygen demand) removal efficiency and the oxidation of ammoniacal nitrogen to nitrate. Further improvements in municipal wastewater purification were achieved using the SPMR. The PMR combines photocatalysis and membrane technologies, enhancing pollutant removal and improving the quality of the purified water. The experimental data is evidenced by the use of an inorganic membrane with a MWCO of 1 kDa, enabling an approximate 15% enhancement in pollutant removal efficiency.

## Introduction

Industrial activities, population growth and urbanization generate a large amount of wastewater, which must be treated before being released into water bodies. Inadequate treatment, as well as improper disposal of water, poses a potentially harmful threat to available freshwater resources. In particular, persistent organic pollutants (POPs) in wastewater represent a potential risk to human health or

biota, even if present at low concentrations.<sup>1</sup> For this reason, the removal of POPs from wastewater has become a global problem.<sup>2</sup> Furthermore, to meet the growing demand for freshwater, wastewater treatment and purification technologies must produce effluents that are not only environmentally safe but also suitable for reuse in appropriate applications, such as agricultural practices.<sup>3</sup> Therefore, POPs in the environment must be reduced to low levels for safe wastewater disposal to prevent environmental and health risks. In effect, the recent EU Directive 3019/2024 regarding the treatment of urban wastewater promotes the reuse of treated wastewaters and imposes during the coming years the adoption in the wastewater treatment plants of processes able to remove organic micropollutants. Conventional biological wastewater treatment plants are not

<sup>a</sup> Institute on Membrane Technology, National Research Council of Italy (ITM-CNR), Cubo 17C, Via Pietro Bucci, Rende 87036, Italy. E-mail: c.algieri@itm.cnr.it

<sup>b</sup> Department of Computer Engineering, Modeling, Electronics and Systems (DIMES), University of Calabria, Via Pietro Bucci, Cubo 42A, Rende 87036, Italy

<sup>c</sup> Department of Environmental Engineering (DIAM), University of Calabria, Via P. Bucci, Cubo 44/A, Rende (CS), Italy



specifically designed to remove recalcitrant pollutants commonly found in urban wastewater. As a result, these contaminants often remain in the treated effluents and are subsequently released into the environment. To address this issue, there is a growing need to develop advanced treatment technologies capable of effectively eliminating persistent pollutants that conventional processes fail to remove.<sup>4</sup> In response, various techniques – such as adsorption, membrane filtration, and advanced oxidation processes (AOPs) – have been investigated for their potential in wastewater purification.<sup>5</sup>

AOPs are advantageous since they allow a partial or total conversion of pollutants due to the generation of highly reactive free radicals.<sup>4–6</sup> AOPs are commonly employed in wastewater treatment to break down persistent pollutants. Recently, electrochemical advanced oxidation processes (e.g. electro Fenton) also gained attention because the use of electrochemical techniques permits the improvement of oxidation efficiency.<sup>7,8</sup>

Photocatalysis is a promising advanced oxidation process (AOP) for wastewater treatment. It involves the use of semiconductor materials that, when exposed to ultraviolet or visible light, generate electron–hole pairs within their lattice structure.<sup>8</sup> Among various photocatalysts, titanium dioxide (TiO<sub>2</sub>) is one of the most widely used due to its low cost, excellent photostability across a broad pH range, low toxicity, and the ability to be recovered and reused after treatment.<sup>9</sup> TiO<sub>2</sub> is active under UV light; when the energy of an incident photon is equal to or greater than its band gap energy (3.2 eV), it is absorbed by the photocatalyst. This absorption excites an electron (e<sup>−</sup>), causing it to migrate from the valence band (VB) to the conduction band (CB), leaving behind a hole (h<sup>+</sup>) in the VB (see eqn (1)). The interaction between (h<sup>+</sup>) and water (H<sub>2</sub>O) in the VB generates hydroxyl radicals (·OH) and the interaction between (e<sup>−</sup>) and dissolved oxygen in the CB generates superoxide ions (O<sub>2</sub><sup>·−</sup>). Subsequently, these species interact with H<sub>2</sub>O to produce new species such as hydroperoxide (H<sub>2</sub>O<sub>2</sub>) radicals. The produced radicals interact with pollutants to generate fewer toxic byproducts such as carbon dioxide (CO<sub>2</sub>) and H<sub>2</sub>O. When electrons and holes are recombined, the photocatalytic activity ends.<sup>9</sup> The generated radicals are highly reactive, enabling the catalysis of various chemical transformations.<sup>10</sup> The oxidation and reduction (redox) reactions are reported in eqn (1)–(3), respectively.

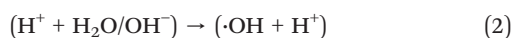


Fig. 1 illustrates the activation mechanism of TiO<sub>2</sub>, where the adsorption of photons with energy exceeding its bandgap leads to the generation of electron–hole pairs (e<sup>−</sup>/h<sup>+</sup>) and other reactive species. These reactive species play a key role in the degradation of pollutants present in urban wastewater.

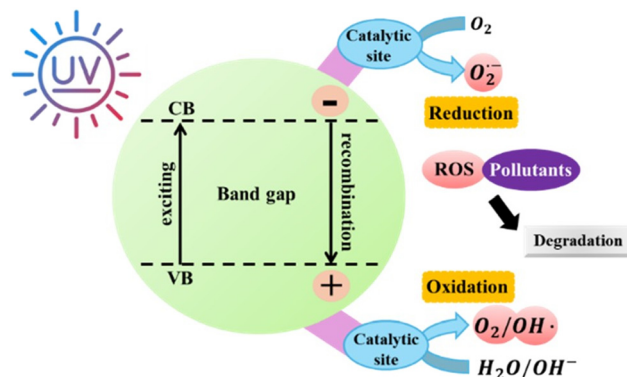


Fig. 1 Pathways of TiO<sub>2</sub> heterogeneous photocatalysis.

However, the large-scale application of photocatalysis is hindered by several challenges, including low photocatalytic activity under sunlight and difficulties in the separation and recycling of the photocatalysts.<sup>11</sup> All these limits can be effectively addressed using photocatalytic membrane reactors (PMRs). The photocatalytic membrane reactor concept integrates photocatalytic technology with membrane processes to enhance the capabilities of traditional photoreactors, while also leveraging the synergistic benefits of both technologies.<sup>12</sup>

The PMR configurations are divided into two principal categories: suspended (also called slurry) and immobilised. In the suspended configuration, titanium dioxide nanoparticles are directly dispersed in the wastewater to be treated, whereas in the immobilised one, the photocatalysts are loaded onto or embedded within the porous structure of the membrane itself.<sup>13</sup> The suspended system allows a good interaction between the reactants and the catalytic sites. However, in this configuration the TiO<sub>2</sub> (mainly at high concentrations) forms agglomerates, which can affect the overall performance of the process. In contrast, the immobilised configuration facilitates easier recovery and reuse of the photocatalyst, as the photocatalytic nanoparticles are retained within or on the membrane structure.<sup>14</sup> Despite this advantage, it is important to highlight that this configuration often suffers very low water flux due to the presence of photocatalytic particles within the membrane, making it less suitable for large-scale applications.

The present study investigates the efficiency of photocatalytic processes for treating real effluents from a conventional municipal wastewater treatment plant. Specifically, the effects of various operating parameters—such as titanium dioxide amount, lamp characteristics, and wastewater composition—on process performance were analysed, with particular focus on chemical oxygen demand (COD) reduction. Based on the most promising photocatalytic results, an inorganic slurry photocatalytic membrane reactor was designed to enhance pollutant degradation and removal. To gain deeper insight into the relationship between process efficiency and light distribution, a finite element model (FEM) was developed to simulate UV light propagation within



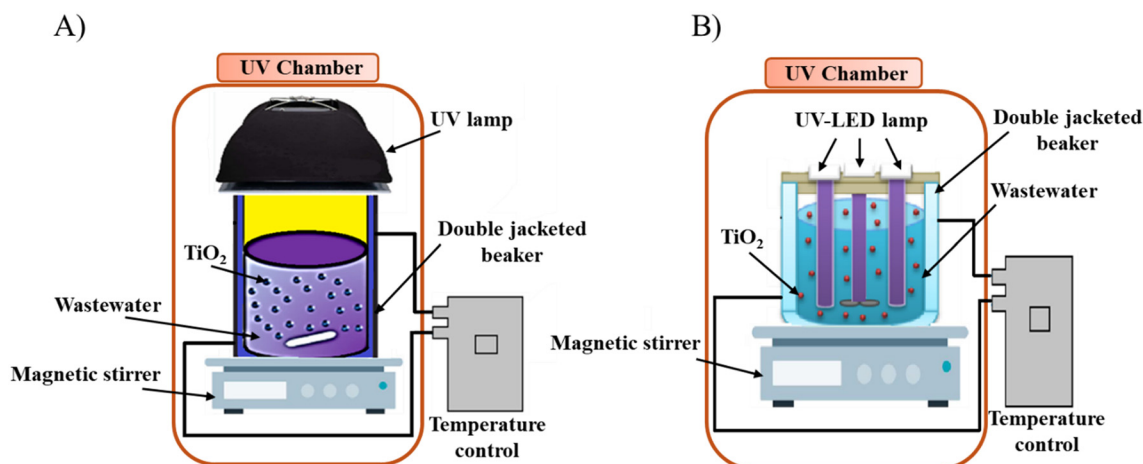


Fig. 2 Scheme of the batch photoreactor (A) with a UV flat lamp (configuration A) and (B) with submerged UV-lamps (configuration B).

the reaction medium for each reactor configuration. Finally, the reusability of the inorganic membrane was assessed.

## Materials and methods

### Materials

For the photocatalytic tests, titanium dioxide ( $\text{TiO}_2$ , particle size  $\sim 350$  nm) was obtained from CARLO ERBA Reagents (Italy). Analytical reagents including potassium dichromate ( $\text{K}_2\text{Cr}_2\text{O}_7$ ), silver sulfate ( $\text{Ag}_2\text{SO}_4$ ), sulfuric acid ( $\text{H}_2\text{SO}_4$ ), 1,10-phenanthroline monohydrate ( $\text{C}_{12}\text{H}_8\text{N}_2\cdot\text{H}_2\text{O}$ ), iron(II) sulfate heptahydrate ( $\text{FeSO}_4\cdot 7\text{H}_2\text{O}$ ), ammonium iron(II) sulfate hexahydrate ( $\text{H}_8\text{FeN}_2\text{O}_8\cdot 6\text{H}_2\text{O}$ ), sodium pentacyanonitrosylferrate(III) dihydrate [ $\text{Na}_2\text{Fe}(\text{CN})_5\text{NO}\cdot 2\text{H}_2\text{O}$ ], sodium dichloroisocyanurate ( $\text{C}_3\text{Cl}_2\text{N}_3\text{NaO}_3$ ), sodium salicylate ( $\text{C}_7\text{H}_5\text{NaO}_3$ ), sodium and potassium tartrate ( $\text{NaKC}_4\text{H}_4\text{O}_6\cdot 4\text{H}_2\text{O}$ ), sodium hydroxide ( $\text{NaOH}$ ), *p*-aminobenzenesulfonamide ( $\text{C}_6\text{H}_8\text{N}_2\text{O}_2\text{S}$ ), hydrochloric acid ( $\text{HCl}$ ), antimonyl tartrate hemihydrate [ $\text{K}(\text{SbO})\text{C}_4\text{H}_4\text{O}_6\cdot \frac{1}{2}\text{H}_2\text{O}$ ], and ammonium heptamolybdate tetrahydrate [ $(\text{NH}_4)_6\text{Mo}_7\text{O}_{24}\cdot 4\text{H}_2\text{O}$ ] were purchased from Sigma-Aldrich (Italy).

Photodegradation experiments were conducted using a 500 W UV lamp (Helios-Quartz Polimer, emission range: 100–400 nm) and submerged UV lamps (Analytik Jena, 6 W each) operating at 365 nm.

### Photocatalytic experiments

Two different UV lamp configurations were employed in the experiment. Configuration A utilized a flat 500 W UV lamp (FUVL) positioned above the photoreactor, while configuration B employed four submerged UV lamps (SUVLs), each with a power of 2.5 W, arranged within the reactor. The entire setup was placed in a UV-protective chamber and positioned on a magnetic stirring plate to minimize  $\text{TiO}_2$  agglomeration and improve photocatalytic efficiency (see Fig. 2).

The operating conditions used during the photocatalytic tests are reported in Table 1.

The collected samples were treated using Imhoff cones for sedimentation, the removal of suspended solid particles, and the deposition of sludge from the wastewater before photodegradation tests.

Photolysis was performed to evaluate the impact of UV light on pollutants present in municipal wastewater, under the same operating conditions (reported in Table 1), without and with a catalyst ( $1.0 \text{ g L}^{-1}$ ).

### Slurry photocatalytic membrane reactor (SPMR)

The slurry photocatalytic membrane reactor (SPMR) consists of a double-jacketed batch reactor coupled with a cross-flow filtration module, as illustrated in Fig. 3. The SPMR operated in a continuous operation mode. The photocatalytic reactor was connected to a decanter and linked to the membrane module.

A cross-flow stirred cell filtration system (DeltaE Srl, Italy) was employed to determine the water flux of the ceramic commercial membrane applying different trans-membrane pressure values ( $\Delta P = 2.5$  bar, 5.0 bar and 7.5 bar). The pure water flux ( $J_{w_i} = \text{L h}^{-1} \text{ m}^{-2}$ ) was determined by using the following equation (eqn (4)):

Table 1 Operating conditions used during the different photocatalytic tests

Reactor configuration	UV lamp power (watt)	Wavelength (nm)	Reaction volume (L)	Reaction time (h)	$\text{TiO}_2$ ( $\text{g L}^{-1}$ )
A	500	UV-A (400–315)	1.6	5	0.5
					0.8
					1
					1.25
					1.5
B	10	UV-A (365)	1.6	5	2.0
					0.5
					0.8
					1
					1.25
					1.5
					2.0



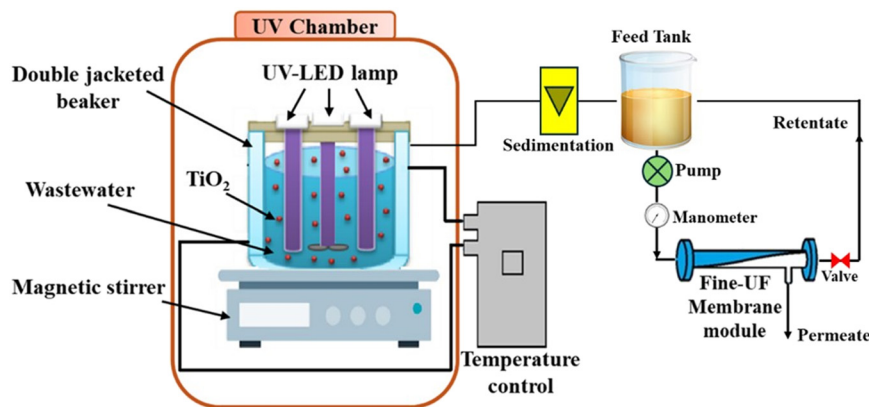


Fig. 3 Scheme of the slurry photocatalytic membrane reactor.

$$J_{w_1} = \frac{V_p}{t \times A} \quad (4)$$

where  $J$  is the water permeate flux ( $J_{w_1}$ ),  $V_p$  is the volume of the permeate collected during time  $t$ , and  $A$  ( $0.06 \text{ m}^2$ ) is the membrane area. The permeability coefficient is determined from the slope of the straight line in a plot of the permeation flux ( $J$ ) versus the pressure difference ( $\Delta P$ ).

The SPMR, operating in cross-flow filtration mode, was employed to purify municipal wastewater. The experiments were conducted at  $25^\circ\text{C}$  for a duration of 5 hours, with the temperature maintained by circulating cold water through the reactor jacket. The pH of the municipal wastewater was  $7.0 \pm 0.3$ . Submerged UV lamps were used for photocatalytic activation. To prevent the formation of  $\text{TiO}_2$  aggregates, the reactor was placed on a magnetic stirring plate and enclosed within a UV chamber. A tubular membrane, mounted in a stainless-steel module (TAMI Industries, Italy), was used, and a transmembrane pressure (TMP) of 5.0 bar was applied while maintaining the temperature at a constant  $25^\circ\text{C}$ . Each experiment was repeated three times to evaluate reproducibility. It is important to highlight that the municipal wastewater samples, provided by the municipal treatment plant, exhibited varying initial COD values.

### Characterization of real wastewater

The real treated municipal wastewater, containing the recalcitrant pollutants, was furnished by a plant located in "Contrada Coda di Volpe"-Rende, Italy (managed by Kratos S. p.A). This is a purification plant with a sewage line composed of preliminary treatments (coarse screening, aerated grit removal), a primary settling phase, an activated sludge process and disinfection, while the sludge line consists of aerobic digestion, post-thickening and mechanical dewatering. The WWTP treats approximately 190 000 P.E. (population equivalent). The samples used during the tests were collected at the outlet of the secondary clarifier units and were stored at  $4^\circ\text{C}$  to avoid alteration. The real municipal and photo-degraded wastewater were analyzed

according to standard methods to determine their composition.<sup>14</sup>

Concentrations of chemical oxygen demand (COD), nitrogen forms ( $\text{N-NH}_4^+$ ,  $\text{N-NO}_2^-$ ,  $\text{N-NO}_3^-$ ) and reactive phosphorus ( $\text{P-PO}_4^{3-}$ ) were measured. COD was determined by means of digestion with  $\text{K}_2\text{Cr}_2\text{O}_7$  and volumetric titration with  $(\text{NH}_4)_2\text{Fe}(\text{SO}_4)_2 \cdot 6\text{H}_2\text{O}$ . Specifically, a volume of 5 ml of wastewater (real and degraded) sample was filtered and placed in the digestion tube with 2.5 ml of  $\text{K}_2\text{Cr}_2\text{O}_7$  (0.025 N) and 7.5 ml of  $\text{Ag}_2\text{SO}_4$ . The prepared solution was placed in a COD reactor, at  $150^\circ\text{C}$  for 2 h for digestion. During this step, the digestion tube was closed with a reflux system equipped with a glass bell, to avoid possible losses of volatile materials from the sample. After this reaction, the samples were cooled, and subsequently, two drops of ferroin solution were added (it was used as an indicator of the colour change during the titration reaction). Additionally, the chilled samples are titrated with standard ferrous ammonium sulphate ( $\text{Fe}(\text{NH}_4)_2(\text{SO}_4)_2$  (0.025 N)) by using a burette of 25 ml.

The COD value ( $\text{mg L}^{-1}$ ) was measured by using eqn (5) as reported below:

$$\text{COD} = \frac{(m_1 - m_2) N 8000}{V} \quad (5)$$

where:

$m_1$  = volume (ml) of ammonium sulphate and iron(II) solution consumed for the blank test.

$m_2$  = volume (ml) of ammonium sulphate and iron(II) solution consumed for the sample.

$N$  = normality of the ammonium sulphate and iron(II) solution used.

8000 = equivalent weight of oxygen multiplied by 1000, to refer the data to the volume of 1 L.

$V$  = volume (ml) of sample used for the analysis.

The concentration of nitrogen in the nitrate ( $\text{N-NO}_3^-$ ), nitrite ( $\text{N-NO}_2^-$ ), and ammonia ( $\text{N-NH}_4^+$ ) forms as well as phosphate ( $\text{P-PO}_4^{3-}$ ) was measured by using a UV spectrophotometer (Thermo Spectronic, Genesys 10 UV, SN 2H7E079002, Rochester, NY USA) at different wavelengths of





420 nm, 543 nm, 690 nm and 882 nm, respectively. Nitrate determination was performed by using the standard method A2 (spectrophotometric determination using sulfanilamide and  $\alpha$ -naphthyl ethylenediamine). 1 ml of sodium salicylate solution was added to the sample in a porcelain capsule, and it was left on the stove at a temperature of 150 °C. After this, 2 ml of H<sub>2</sub>SO<sub>4</sub> and 15 ml of distilled water were added to the capsule and left to cool. At the end, 15 ml of Seignette salt was added for the determination to the spectrophotometer. The nitrite was determined using the standard method A1 (spectrometric determination using sodium salicylate). A volume of 200  $\mu$ L of sulphanilamide (SA) solution and 200  $\mu$ L of naphthyl ethylenediamine (NEDA) solution were added to the sample. After a few minutes it is possible to analyse the variation in terms of N-NO<sub>2</sub> concentration by measuring the absorbance on the spectrophotometer. The ammonia concentration was evaluated using the standard method A1 (spectrophotometric determination of indophenol). A volume of 400  $\mu$ L of a solution of sodium nitroprusside/sodium salicylate and 400  $\mu$ L of a solution of sodium dichloroisocyanurate/sodium citrate were added to the sample and left to react for 2 hours covered with parafilm. After this, the variation in terms of N-NH<sub>4</sub><sup>+</sup> concentration can be determined by measuring the absorbance on the spectrophotometer. Phosphate determination was carried out using standard method A1 (dosage of phosphorus as soluble orthophosphate). A volume of 300  $\mu$ L of an ammonium molybdate solution and 300  $\mu$ L of a potassium antimonyl tartrate solution were added to the treated wastewater sample, and the reduction of P-PO<sub>4</sub><sup>3-</sup> can be determined by measuring the absorbance on the spectrophotometer.

### Finite element modelling

Based on the experimental procedures described above, a 3D model is proposed, to compare the two configurations, where UV ray profiles through the reactor media have been calculated along with the power carried in each point of the reaction domain. For each case, the total power provided by the initial rays was set as the actual total power of the lamp. The model intent is to give a quantified hint on how much of the provided power reaches the reaction domain, thus making it available for photocatalysis activation.

FEM has been conducted through the software *COMSOL Multiphysics* to calculate the propagation of the electromagnetic radiation in the reactors. The main assumption of the used governing equations is that the wavelength is much smaller than the characteristic dimensions of the system (high-frequency approximation); by this assumption Maxwell's equations can be reduced to the Eikonal equation, which describes the path of the optical phase  $\varphi$  expressed as  $\nabla\varphi = n(r)$ , where  $n(r)$  is the refractive index of the medium.

Ray paths are traced according to the following ray equation (eqn (6)):

$$\frac{d}{ds} \left( n(r) \frac{dr}{ds} \right) = \nabla n(r) \quad (6)$$

where  $r(s)$  is the ray position vector parameterized by the arc length  $s$ . This second-order ODE well describes the evolution of a ray through non-homogeneous media. The model includes optical phenomena like reflection, refraction, polarization, and absorption. The study has been set as time-dependent, in a time range from 0 to 1 ns, enough to embrace the full development of the phenomena, while ray intensity attenuation has been calculated as governed by the Beer-Lambert law, which describes absorption, for each material domain, by using eqn (7):

$$I(s) = I_0 e^{-\int_0^s \alpha(r(s')) ds'} \quad (7)$$

where  $\alpha$  is the absorption coefficient of the medium.

External walls of the reactor units are set to let any incident rays disappear, in order to eliminate any (at least) third generation low-powered rays that may be generated from the furthest refraction in the domain, while any other material discontinuity in the model that generates optical reflections has been considered; by this way, nearfield second-generation (and even higher generation) rays, whose path and power depend on the material properties, are calculated.

Material properties for air, water, optical glass and borosilicate glass, particularly the refractive indexes, were retrieved from the available literature.<sup>15</sup>

It is worth considering that, to give a clearer view of how much of the light power generated by the lamp actually reaches the reaction bulk, for configuration B specific boundaries, representing a plausible entrance to the reaction medium bulk, have been set to “freeze” the incident rays to have them highlighted. In addition, to lower the computational needs, configuration B has been modeled just for a quarter of the total domain: a single lamp providing a quarter of the total power along with a quarter of the reaction volume surrounding it has been modeled; here the reduced domain is identified by two symmetry planes (mutually perpendicular with respect to the  $x$ - $y$  plane) passing through the center of the reactor. For configuration A, the reactor has been modeled with its glass domain, air and water heads, and the lamp power has been set scattering downwards from the upper boundary of the air domain, while for configuration B, the model consists of reactor walls, a water domain, a tube-like lamp domain, and air and optical glass domain annuluses surrounding the lamp. In Fig. 4 the geometrical representations of the models, along with the relative calculation meshes, are reported.

### Kinetic studies

The kinetics of photocatalytic degradation were studied, and the linear model equations are reported below:



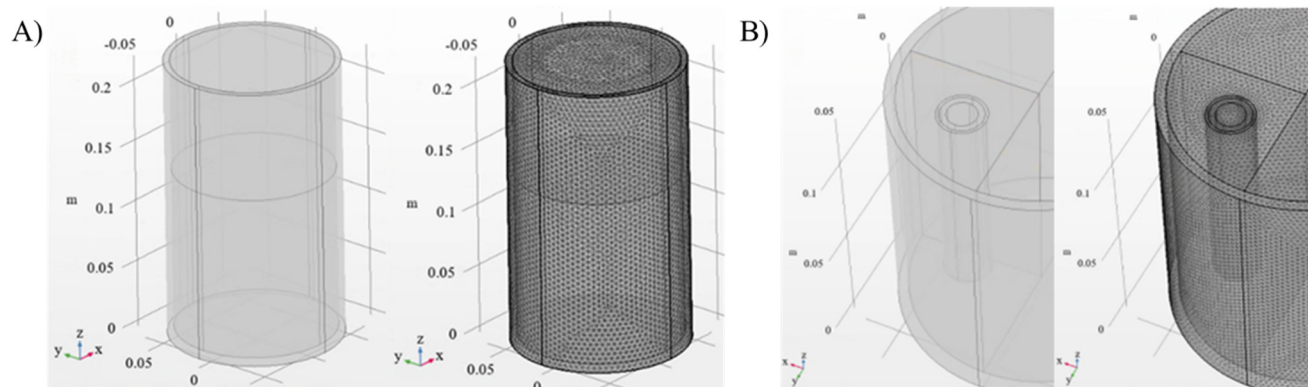


Fig. 4 Graphical representation of the modeled configuration A (A) and configuration B (B), together with the calculation mesh generated.

The following equation (eqn (8)) describes the zero-order kinetic model:

$$C_0 - C_t = K_0 t \quad (8)$$

where  $C_0$  is the initial COD value ( $\text{mg L}^{-1}$ ),  $C_t$  is the COD value ( $\text{mg L}^{-1}$ ) during the time,  $K_0$  ( $\text{mg L}^{-1} \text{min}^{-1}$ ) is the zero-order constant, and  $t$  is the time of the reaction.

The first-order and second-order kinetics are described using eqn (9) and (10), respectively:

$$\ln \frac{C_0}{C_t} = K_1 t \quad (9)$$

where  $C_0$  is the initial COD value ( $\text{mg L}^{-1}$ ),  $C_t$  is the COD value ( $\text{mg L}^{-1}$ ) during the time,  $K_1$  ( $\text{min}^{-1}$ ) is the first-order constant, and  $t$  is the time of the reaction.

$$\frac{1}{C_t} - \frac{1}{C_0} = K_2 t \quad (10)$$

where  $C_0$  is the initial COD value ( $\text{mg L}^{-1}$ ),  $C_t$  is the COD value ( $\text{mg L}^{-1}$ ) during the time,  $K_2$  ( $(\text{mg L}^{-1})^{-1} \text{min}^{-1}$ ) is the second-order constant, and  $t$  is the time of the reaction.

Eqn (11) and (12) represent the pseudo first-order and pseudo second-order kinetic models, respectively.

$$\ln \frac{C_0 - C_f}{C_t - C_f} = K_1^* t \quad (11)$$

where  $C_0$  is the initial COD value ( $\text{mg L}^{-1}$ ),  $C_t$  is the COD value ( $\text{mg L}^{-1}$ ) during the time,  $C_f$  is the final COD value ( $\text{mg L}^{-1}$ ),  $K_1^*$  ( $\text{min}^{-1}$ ) is the pseudo first-order constant, and  $t$  is the time of the reaction.

$$\frac{1}{(C_t - C_f)} - \frac{1}{(C_0 - C_f)} = K_2^* t \quad (12)$$

where  $C_0$  is the initial COD value ( $\text{mg L}^{-1}$ ),  $C_t$  is the COD value ( $\text{mg L}^{-1}$ ) during the time,  $C_f$  is the final COD value ( $\text{mg L}^{-1}$ ),  $K_2^*$  ( $(\text{mg L}^{-1})^{-1} \text{min}^{-1}$ ) is the pseudo second-order constant, and  $t$  is the time of the reaction.

### Membrane reuse and fouling

Three different flux measurements were performed to evaluate fouling resistance during experiments with real photo-treated wastewater. First, the initial pure water flux ( $J_1$ ) was measured after 10 minutes. Subsequently, during wastewater filtration, the flux ( $J_2$ ) was recorded after 1.5 hours. Finally, after cleaning the membrane with distilled water to remove inorganic and organic contaminants, the pure water flux ( $J_{w_2}$ ) was again measured. The membrane's fouling characteristics were evaluated by calculating the flux decline ratio (FDR%) and flux recovery ratio (FRR%) using eqn (13) and (14) given below.

$$\text{FDR}\% = \frac{J_1 - J_2}{J_1} \times 100 \quad (13)$$

$$\text{FRR}\% = \frac{J_{w_2}}{J_{w_1}} \times 100 \quad (14)$$

The fouling impact on the ceramic membrane was further analyzed with the total fouling ratio ( $R_T$ ), reversible fouling ratio ( $R_{\text{rev}}$ ), and irreversible fouling ratio ( $R_{\text{irrev}}$ ) using eqn (15)–(17) provided below.

$$R_T\% = 1 - \frac{J_2}{J_{w_1}} \times 100 \quad (15)$$

$$R_{\text{rev}}\% = \frac{J_{w_2} - J_2}{J_{w_1}} \times 100 \quad (16)$$

$$R_{\text{irrev}}\% = \frac{J_{w_1} - J_{w_2}}{J_{w_1}} \times 100 \quad (17)$$

### Membrane characterization

The  $\text{TiO}_2$  nanoparticles were characterized using an X-ray diffractometer (Rigaku MiniFlex 600, Japan) with  $\text{CuK}\alpha$  (wavelength of  $1.5406 \text{ \AA}$ ) radiation generated at 20 mA and 40 kV. The powdered samples were scanned at  $0.02 \text{ } 2\theta$  steps at a rate of  $1^\circ \text{ min}^{-1}$  between  $10^\circ$  and  $80^\circ$  ( $2\theta$  angle range).



Morphological analyses of the tubular inorganic membrane were carried out using an ultra-high-resolution scanning electron microscope (ZEISS instrument, Carl Zeiss Microscopy Ltd. Cambridge CB1 3JS (Ser. No. EVO10-16-41), United Kingdom).

## Results and discussion

### Degradation of persistent pollutants by the batch photoreactor and SPMR

This study was performed on treated effluent from a municipal wastewater treatment plant (WWTP) employing a conventional activated sludge process. The characteristics of the effluent indicated that the main parameters were below the limits established by Italian regulations for discharge into surface water bodies, as outlined in D.lgs. 152/06 (Environmental Regulations, 2006).

In particular, the effluent showed low concentrations of chemical oxygen demand (COD), and the WWTP demonstrated partial removal of nitrogen species, as well as a relatively low phosphorus concentration (COD: 77.8 mg L<sup>-1</sup>; N-NH<sub>4</sub><sup>+</sup>: 6.65 mg L<sup>-1</sup>; P-PO<sub>4</sub><sup>3-</sup>: 0.83 mg L<sup>-1</sup>).

Despite the high treatment efficiency of the wastewater treatment plant (WWTP), residual concentrations of contaminants were still detected. In particular, the remaining chemical oxygen demand (COD) in the effluent is mainly attributed to poorly biodegradable and persistent organic compounds that are not easily removed by conventional treatment methods.

The photocatalytic experiments were conducted to assess the capability of heterogeneous photocatalysis in breaking down the residual, low-biodegradability COD fraction remaining in the effluent. Various operating conditions influence the efficiency of heterogeneous photocatalysis. Among them, catalyst loading plays a particularly important role. In this study, the effect of catalyst concentration was investigated as a key parameter impacting photocatalytic performance. An optimal amount of catalyst helps to minimize particle agglomeration, thereby maximizing the

number of available active sites and improving degradation efficiency. Conversely, at higher TiO<sub>2</sub> concentrations, the increased turbidity of the suspension reduces light penetration, limiting the activation of the photocatalyst. Additionally, excessive catalyst loading can lead to the formation of aggregates, which decreases the effective surface area and further restricts access to active sites.<sup>16–18</sup> Considering this aspect, the TiO<sub>2</sub> concentration impact on photocatalytic performance was assessed. Five experiments were performed, varying the TiO<sub>2</sub> concentration from 0.5 to 2.0 g L<sup>-1</sup>, while keeping all other operating conditions constant (initial COD level, temperature, and reaction time). The results demonstrated that catalytic activity improved with increasing TiO<sub>2</sub> concentration, reaching a peak at 1.5 g L<sup>-1</sup> in configuration A and 1.0 g L<sup>-1</sup> in configuration B. The highest COD removal efficiencies observed were 45% for configuration A at 1.5 g L<sup>-1</sup>, and 43% for configuration B at 1.0 g L<sup>-1</sup>. However, further increases in catalyst concentration led to a decline in process performance in both configurations, likely due to the aforementioned light attenuation and aggregation effects (see Fig. 5a and b). The decrease in recalcitrant pollutant degradation can be attributed to the formation of photocatalyst clusters. This phenomenon directly affects the generation of radical species responsible of pollutant degradation.<sup>19–21</sup> Therefore, comparing the two system configurations, the photocatalytic batch reactor with submerged UV lamps showed superior process performance. The obtained results can be explained by considering that submerged UV lamps are placed directly in the batch of the reaction, ensuring a uniform light distribution throughout the suspension.<sup>22</sup> In contrast, the external flat UV lamp exhibited limitations in light penetration, irregular light distribution, and reduced photocatalytic efficiency.<sup>19,20</sup> In addition, using a reduced amount of photocatalysts minimized suspension turbidity, thereby enhancing light diffusion and preventing cluster formation. These factors mutually contribute to enhancing photodegradation performance.<sup>13,23–29</sup>

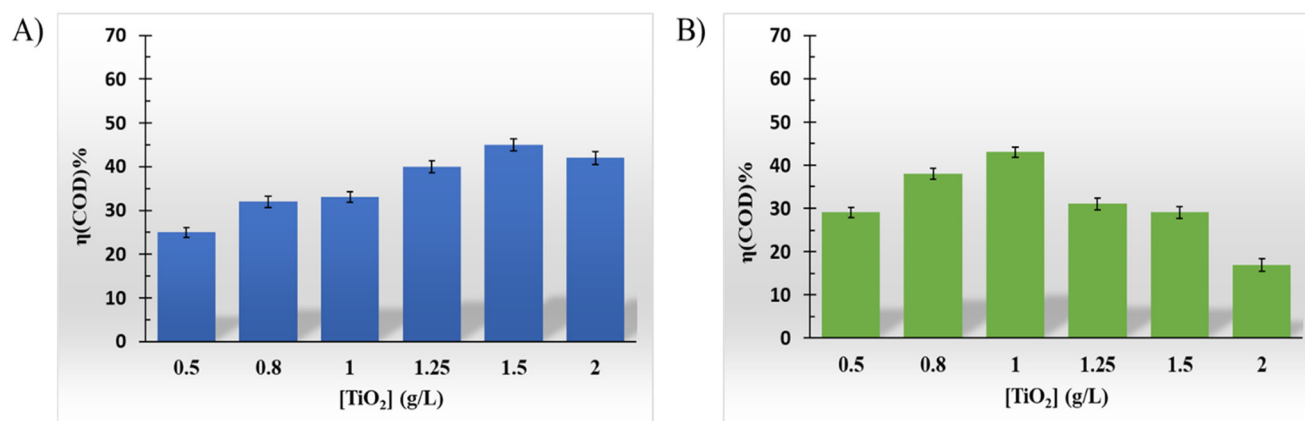
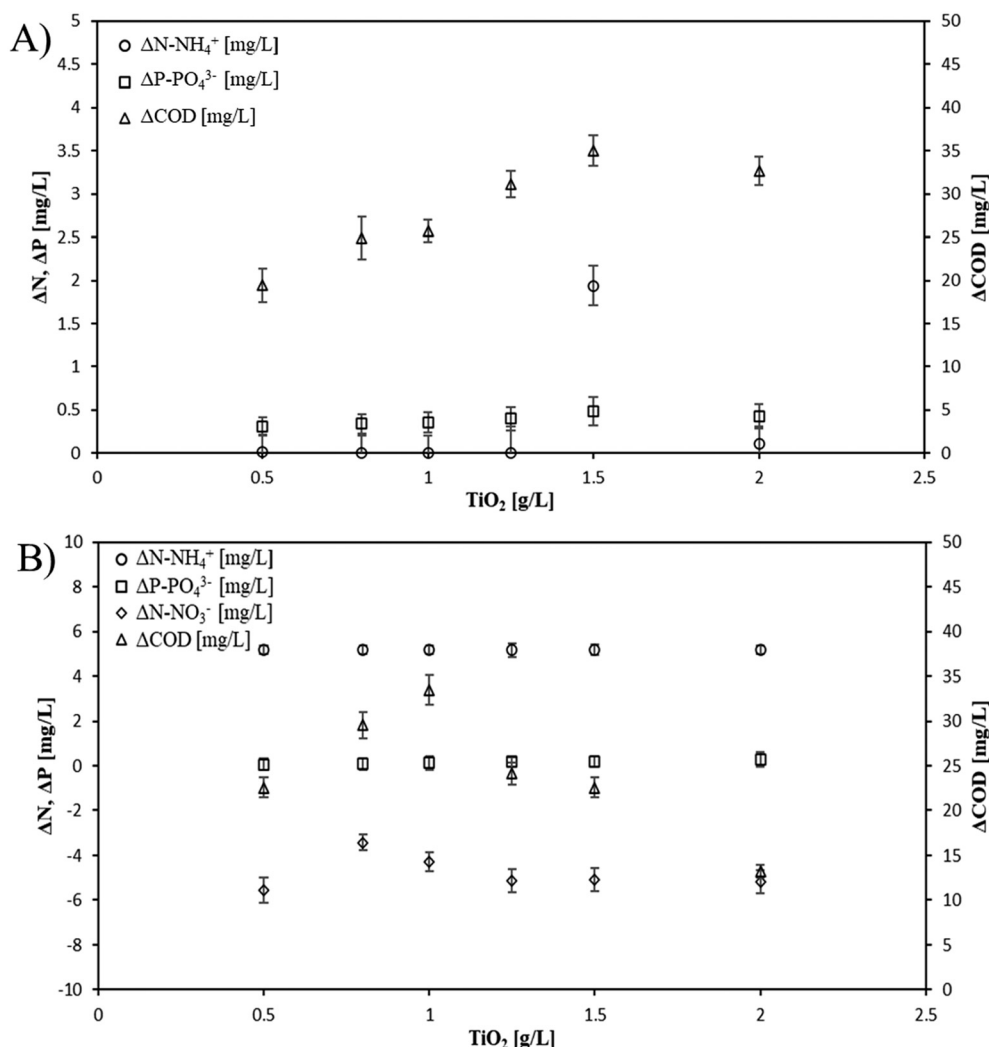


Fig. 5 Effect of TiO<sub>2</sub> concentration on the COD removal for (A) FUVL and (B) SUVL configurations.





**Fig. 6** Variation in influent and effluent wastewater characteristics using the two photoreactor configurations: (A) batch photoreactor with a UV flat lamp, and (B) batch photoreactor with submerged UV lamps. Key parameters monitored include COD, N-NH<sub>4</sub><sup>+</sup>, N-NO<sub>2</sub><sup>-</sup>, N-NO<sub>3</sub><sup>-</sup>, and P-PO<sub>4</sub><sup>3-</sup>. Discharge limits are as follows: COD: 125 mg L<sup>-1</sup> (wastewater-discharge limit values. "All.5, P. Terza, D.lgs. n.152 del 03.04.06", Table 1 "Limiti di emissione per gli impianti di acque reflue urbane"); N-NH<sub>4</sub><sup>+</sup> = 15 mg L<sup>-1</sup>; N-NO<sub>2</sub><sup>-</sup> = 0.6 mg L<sup>-1</sup>; N-NO<sub>3</sub><sup>-</sup> = 20 mg L<sup>-1</sup>; P-PO<sub>4</sub><sup>3-</sup> = 0.6 mg L<sup>-1</sup> (wastewater-discharge limit values. "All.5, P. Terza, D.lgs. n.152 del 03.04.06", Table 3 "Valori limiti di emissione in acque superficiali e in fognatura").

The variation in influent and effluent wastewater characteristics using the two photoreactor configurations (A: batch photoreactor with a UV flat lamp and B: batch photoreactor with submerged UV lamps) has been reported in Fig. 6a and b. It is important to evidence that variation for some chemical species (*e.g.* nitrite and nitrate in Fig. 6a and nitrite in Fig. 6b) is not reported because no variation was observed.

Ammonia (NH<sub>4</sub><sup>+</sup>) is an important parameter to evaluate water quality. The removal of ammoniacal nitrogen is typically achieved through processes such as nitrification and denitrification, which convert ammonia into less harmful chemical species. Elevated nitrogen levels in water have serious negative impacts on both human health and the environment (including eutrophication, toxicity to aquatic life, and contributions to climate change). During the

photocatalytic degradation, free radicals convert ammonia into other nitrogen species, such as nitrate (NO<sub>3</sub><sup>-</sup>).<sup>26</sup>

The results reported in Fig. 6a and b indicated that the immersed lamps promoted the oxidation of ammonia into nitrate (NO<sub>3</sub><sup>-</sup>) species. The lamp immersed in the wastewater favoured an optimization of the light distribution that ensured a continuous activation of the catalytic particles and so a rise of the reactive species was observed. Therefore, the ammonia is converted into nitrate (a less toxic form of nitrogen) with an improvement in the overall wastewater treatment. In addition, the flat UV lamps were not effective in promoting the oxidation of ammonia into less harmful chemical species.

The immersed lamp setup thus provided different advantages, improving the efficiency and sustainability of the photocatalytic process. In addition, a possible way to





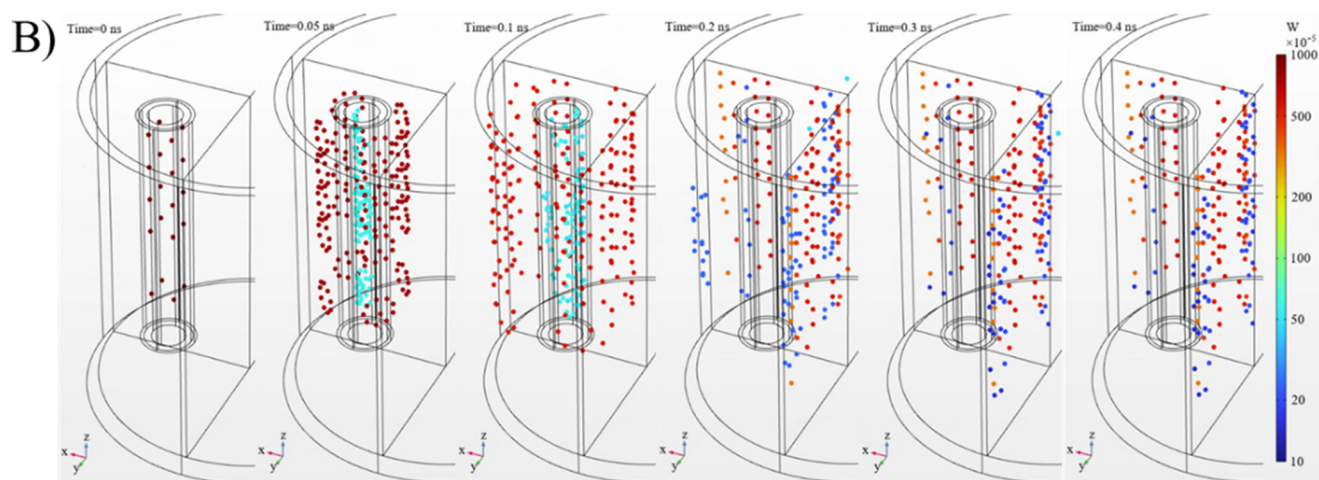


Fig. 7 FEM results: (A) ray position and power on different simulation times (0–1 ns) for configuration A. (B) Ray position and power on different simulation times (0–1 ns) for configuration B (incident rays are “frozen” onto the two symmetry planes cutting the domain).

**Table 2** Bulk power and lighting efficiency calculated by FEM for the two reactor configurations

Configuration	Lamp power [W]	$P_r$ [W]	$\eta_r$ [%]
A	500	2.864	0.57
B	10	2.326	23.26

eliminate the nitrate produced (which in some cases exceeds the legal limits) is biological denitrification.<sup>27</sup> The latter is recognised as the most effective and environmentally sustainable method for removing nitrate ( $\text{NO}_3^-$ ) from wastewater.<sup>27</sup> This process reduces nitrate to gaseous nitrogen ( $\text{N}_2$ ), which is safely released into the atmosphere. It is extensively applied in both municipal and industrial wastewater treatment systems.

The photolysis test performed on wastewater with an initial COD value of  $56.19 \text{ mg L}^{-1}$  showed a removal efficiency of 11.14%. In the presence of the catalyst, the removal efficiency increased to 33.35%. This indicates that the actual catalytic performance contributed approximately 22.21% to the overall removal efficiency.

Results obtained with the finite element modelling are graphically presented in terms of ray power and ray position, respectively in Fig. 7a and b, for both configurations A and B, at different times spanning from 0 to 1 ns.

A consistent interpretation of the results is provided in Table 2, which reports both the total light power entering the reaction bulk ( $P_r$ ) and the lighting efficiency ( $\eta_r$ ), expressed as the ratio of  $P_r$  to the total power supplied by the lamp system.

It is clear how in terms of  $P_r$ , the two systems run fairly on the same numbers, with values for configuration A slightly higher than configuration B; this result provides consistency with the experimental results discussed above. Still, in terms of efficiency, configuration B has by far higher lighting efficiency than configuration A, setting a hint on further pilot scale developments of the entire process. The last consideration is made clear considering that a vast portion of lightning power gets lost by scattering and nonoptimal set up, so that the assertions made for the experimental results proposed in Tables 3 and 4 can be confirmed. Therefore, the immersed lamp configuration, which results in a better light distribution, responds with an improved catalytic activity. As a direct consequence positive effects like the ammonia to nitrate conversion can be linked to reactor geometrical configuration choices.

The COD removal efficiency as a function of time at different  $\text{TiO}_2$  concentrations for both configurations is reported in Fig. 8a and b. It can be observed that COD removal increased over time, reaching a plateau after approximately 3.3 hours. This time-dependent behaviour is influenced by the availability of active sites, the formation of titanium dioxide clusters, and the generation of intermediate compounds that may be more resistant to further degradation, thereby slowing the overall COD removal rate.<sup>28</sup>

The experimental results obtained using the optimal photocatalyst concentrations for both reactor configurations were analysed using various kinetic models. The most suitable model for the photodegradation process was identified based on the correlation coefficient ( $R^2$ ), with the corresponding results summarized in Table 3. The kinetic analysis indicated that the second-order model provided the best fit for both the photocatalytic batch reactor with a flat UV lamp and the reactor equipped with submerged UV lamps. These findings suggest that adsorption plays a significant role in the photodegradation process. In particular, the second-order kinetics imply that the reaction rate is proportional to the square of the reactant concentration, indicating that surface interactions – likely involving chemisorption – dominate the degradation mechanism.<sup>29</sup>

Various experiments were carried out using wastewater samples with different initial COD values. This is explained considering that municipal wastewater exhibits a wide range of initial COD values because of it is a mixture of domestic, industrial, and commercial discharges. The relative contributions of these sources can vary over time, resulting in significant fluctuations in organic load. The results, shown in Fig. 9a, indicate that COD removal efficiency decreases as the initial COD concentration increases. This trend can be attributed to the increased turbidity of the suspension, which limits light penetration. Furthermore, the adsorption of organic pollutants onto the catalyst surface hinders the generation of reactive radical species.<sup>30</sup> To enhance pollutant removal, a slurry inorganic photocatalytic membrane reactor (SPMR) was utilized. The SPMR integrates photocatalysis with membrane filtration, enabling simultaneous degradation of contaminants and physical separation of catalyst particles, thereby improving overall treatment efficiency. While inorganic membranes tend to be more costly than their polymeric counterparts, they provide significant benefits that

**Table 3** Kinetics data at different  $\text{TiO}_2$  concentrations

$[\text{TiO}_2]$ ( $\text{mg L}^{-1}$ )	Zero order		First order		Second order		Pseudo-first order		Pseudo-second order	
	$K_0$	$R^2$	$K_1$	$R^2$	$K_2$	$R^2$	$K_{1*}$	$R^2$	$K_{2*}$	$R^2$
1.5	$2.0 \times 10^{-1}$	0.92	$3.3 \times 10^{-3}$	0.95	$6.0 \times 10^{-5}$	<b>0.97</b>	$2.6 \times 10^{-2}$	0.90	$1.3 \times 10^{-1}$	0.70
1.0	$1.8 \times 10^{-1}$	0.96	$2.9 \times 10^{-3}$	0.98	$5.0 \times 10^{-5}$	<b>0.99</b>	$2.25 \times 10^{-2}$	0.90	$5.0 \times 10^{-2}$	0.69

$K_0$  ( $\text{mg L}^{-1} \text{ min}^{-1}$ ),  $K_1$  ( $\text{min}^{-1}$ ),  $K_2$  ( $(\text{mg L}^{-1})^{-1} \text{ min}^{-1}$ ),  $K_{1*}$  ( $\text{min}^{-1}$ ) and  $K_{2*}$  ( $(\text{mg L}^{-1})^{-1} \text{ min}^{-1}$ ) are the kinetic constant for zero order, first-order, second order, pseudo-first order and pseudo-second order models, respectively.



Table 4 TiO<sub>2</sub>-based photocatalytic treatments: comparative analysis

Photocatalyst	Catalyst Conc. (g L <sup>-1</sup> )	Aeration flow rate (L min <sup>-1</sup> )	Power UV lamp [W]	Reaction time [h]	T [°C]	Reactor configuration	Membrane	Wastewater type	Initial COD (mg L <sup>-1</sup> )	COD removal efficiency (η%)	Ref.
TiO <sub>2</sub>	8.0	1.225	36	0.5	25	Flat	—	Oily refinery wastewater	4000	88	34
TiO <sub>2</sub> + H <sub>2</sub> O <sub>2</sub>	1.2	—	88	2	38	Submerged	—	Pharmaceutical wastewater	168–240	33	35
TiO <sub>2</sub>	0.1	—	250	2.5	—	Flat	—	Municipal sewage	620	12	36
TiO <sub>2</sub>	1.0	—	400	—	50	Flat	—	Petroleum refinery effluent	8200	60	37
TiO <sub>2</sub>	0.10	—	—	2.5	—	—	—	Real greywater	620	54	38
TiO <sub>2</sub>	1.0	—	10	5	25	Submerged	—	Treated municipal wastewater <sup>a</sup>	78	43	This work
TiO <sub>2</sub>	0.12	—	8	—	—	Submerged	RO	Oil refinery wastewater	45	56	39
TiO <sub>2</sub>	1.0	—	10	5	25	Submerged	FINE UF	Treated municipal wastewater <sup>a</sup>	78	58	This work

<sup>a</sup> Treated municipal wastewater before being discharged into river (water containing recalcitrant pollutants).

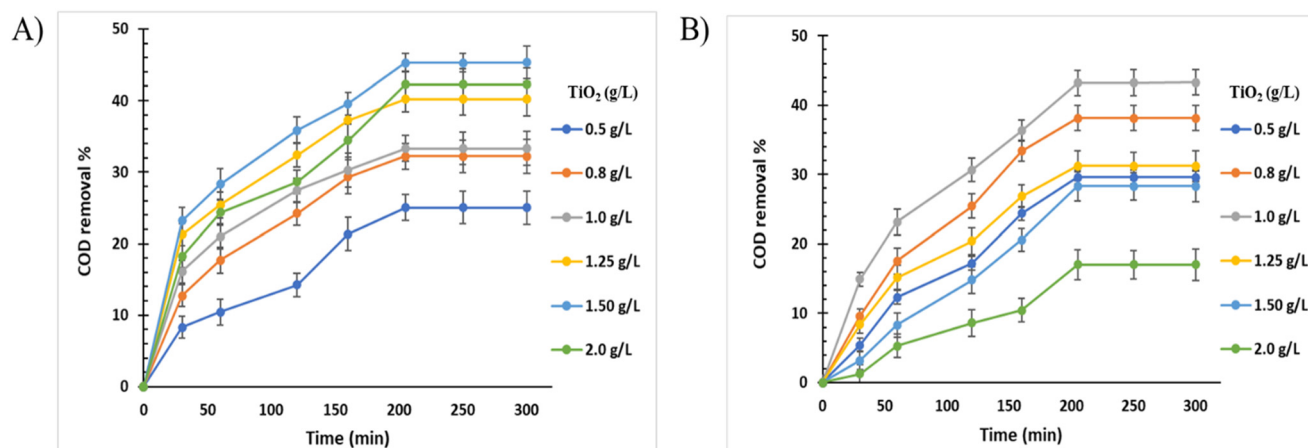


Fig. 8 Effect and COD removal vs. time: (A) for FULV and (B) for SUVL configurations.

justify the investment.<sup>31</sup> These advantages include superior resistance to harsh chemical cleaning agents and repeated backwashing cycles, which are essential for maintaining membrane performance and “long life” in wastewater treatment applications. Additionally, inorganic membranes exhibit exceptional mechanical stability, allowing them to operate under a wide range of pressures without deformation or loss of integrity.<sup>31</sup> The results for COD removal efficiency (η%) obtained with the SPMR are shown in Fig. 9b. The experimental data evidenced that the use of an inorganic membrane with a MWCO of 1 kDa permitted an improvement in pollutant removal of about 15% to be obtained. This membrane is capable of separating particles and molecules larger than 1000 Da while smaller molecules pass through it. The integration of a nanofiltration membrane into the SPMR system will significantly enhance wastewater treatment efficiency by combining the potent

pollutant-degradation capability of photocatalysis with the specific separation performance of nanofiltration. This synergistic combination yields cleaner effluent and a more resource-efficient treatment process. The reusability of the membrane was also evaluated, considering the PMR test 1. After each cycle, the membrane was washed with distilled water before introducing a new photo-treated wastewater and the results are illustrated in Fig. 9c.

After the first cycle, the flux recovery ratio (FRR) was 97.37%, indicating only a slight flux reduction of approximately 2.27%. However, the flux decline ratio (FDR) increased with each successive cycle, reflecting the progressive fouling of the membrane. A decrease in reversible fouling ( $R_{rev}$ ) was observed over time, suggesting that a growing portion of the fouling became irreversible with each filtration cycle. This irreversible fouling ( $R_{irr}$ ) is likely due to the strong adsorption of pollutants onto the



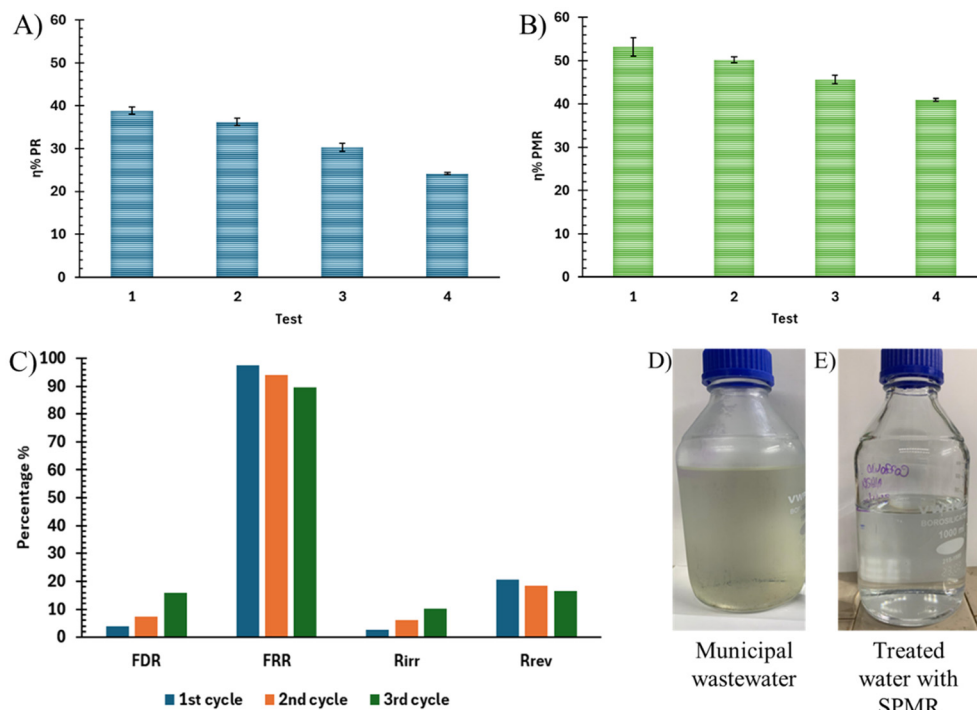


**Fig. 9** COD removal efficiency in: (A) PR and (B) SPMR (operating conditions:  $T = 25\text{ }^{\circ}\text{C}$ ; TEST 1:  $\text{COD}_i = 36.14\text{ mg L}^{-1}$ ; TEST 2:  $\text{COD}_i = 50.19\text{ mg L}^{-1}$ ; TEST 3:  $\text{COD}_i = 56.34\text{ mg L}^{-1}$ ; TEST 4:  $\text{COD}_i = 103.08\text{ mg L}^{-1}$ ;  $\text{TiO}_2 = 1.0\text{ g L}^{-1}$  (for PR),  $\Delta P = 5\text{ bar}$  (for SPMR). Membrane reuse and fouling: (C) FRR, FDR, Rrev., and Rirr., of SPMR (TEST 1:  $\text{COD}_i = 36.14\text{ mg L}^{-1}$ ;  $T = 25\text{ }^{\circ}\text{C}$ ,  $\Delta P = 5.0\text{ bar}$ ). Pictures of (D) municipal partially treated wastewater and (E) clean wastewater by the SPMR.

membrane surface and within its pores.<sup>32</sup> The results showed that the inorganic membrane is less susceptible to fouling due to its high chemical stability and hydrophilic nature, which permit the reduction of the accumulation of organic pollutants on the surface and within the membrane pores.<sup>33</sup>

Table 4 reports a comprehensive comparison between the current study and previously published works involving  $\text{TiO}_2$ -based photocatalytic treatments of various real wastewater types.

In particular, in this study, a COD removal efficiency of 43% was achieved using  $\text{TiO}_2$  alone, and 58% when coupled with a FINE-UF membrane, treating municipal wastewater with an initial COD of only  $78\text{ mg L}^{-1}$ . These results are particularly significant when compared to other studies that often required higher catalyst concentrations (up to  $8\text{ g L}^{-1}$ ), more intense UV irradiation (up to  $400\text{ W}$ ) and higher temperature values. Furthermore, the integration of membranes, particularly FINE-UF, substantially improved treatment performance, validating the potential of hybrid photocatalytic-membrane systems for enhancing pollutant removal. In addition, the RO membrane exhibited operational drawbacks due to membrane fouling, primarily caused by the accumulation of organic matter and  $\text{TiO}_2$  aggregates. The fouling not only causes reduction of the membrane permeability but also shortens membrane life and increases operational costs.

### Photocatalyst and ceramic membrane characterization

Three titanium dioxide polymorphs are found in nature: anatase, rutile and brookite, of which anatase showed higher photocatalytic activity compared to rutile and brookite.<sup>40</sup> The XRD pattern of the commercial  $\text{TiO}_2$  (calcined at  $500\text{ }^{\circ}\text{C}$  for 1 h) used in this work showed only the anatase phase (see Fig. 10a).

In Fig. 10(b–d), the cross-section showed the microporous  $\text{TiO}_2$  support (at the bottom), two  $\text{TiO}_2$  intermediate layers and a very thin nanoporous  $\text{TiO}_2$  active layer on the top.

## Conclusions

This study distinguishes itself from much of the existing literature by focusing on the photocatalytic degradation of persistent organic pollutants in real urban wastewater, rather than in synthetic model solutions. This approach enhances the relevance and practical applicability of the findings, particularly in evaluating the performance of titanium dioxide-based slurry reactors under complex, variable wastewater conditions.

Initially, the photodegradation of persistent organic pollutants in real treated urban wastewater was assessed using a  $\text{TiO}_2$ -based batch photoreactor. Two reactor configurations were compared: one employing a flat UV lamp and the other equipped with submerged UV lamps. Experimental results showed that the submerged lamp configuration significantly exhibited superior performance





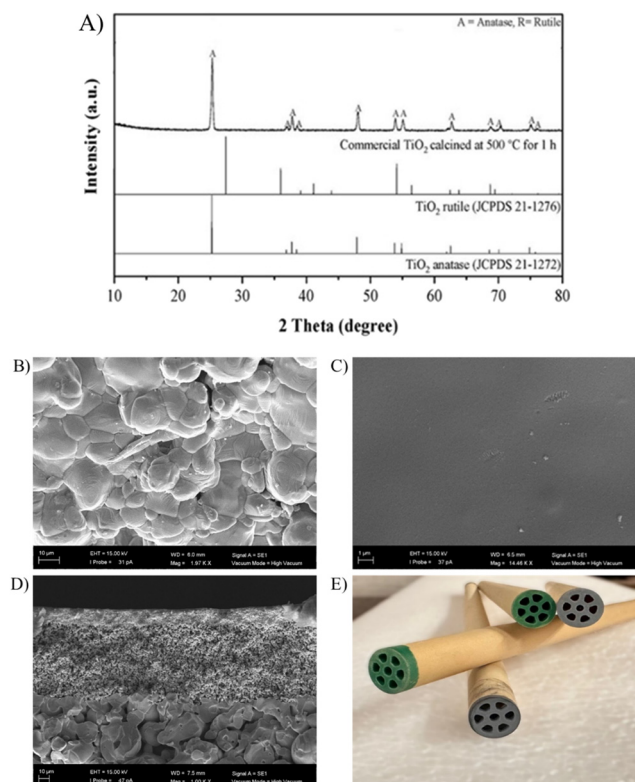


**Fig. 10** (A) XRD pattern of commercial  $\text{TiO}_2$ . SEM images of the multichannel  $\text{TiO}_2$  membrane used for the SPMR: (B) external top-view, (C) internal top-view, (D) cross-section and (E) picture of the multichannel  $\text{TiO}_2$  membrane.

compared to the flat lamp setup, demonstrating higher COD removal and enhanced oxidation of ammoniacal nitrogen to nitrate. To elucidate the role of light distribution, a finite element model (FEM) was developed to simulate the UV light propagation within the reaction medium. The simulation confirmed that the submerged lamps provide superior light distribution, resulting in increased photocatalytic activity.

Further improvements in treatment performance were achieved through the implementation of a slurry photocatalytic membrane reactor (SPMR). The use of a multichannel tubular  $\text{TiO}_2$  membrane with a molecular weight cut-off (MWCO) of 1 kDa led to a 15% increase in pollutant removal efficiency, demonstrating the advantage of combining photocatalysis with membrane filtration. The integration of a nanofiltration unit into the SPMR system offers an additional layer of selectivity, allowing for the retention of larger degradation by-products while permitting smaller, less harmful molecules to pass through. This synergistic combination of photocatalysis and membrane separation leads to cleaner effluents and a more resource-efficient overall process.

In conclusion, this study demonstrates that PMRs – when carefully designed and optimized – represent a promising, integrative approach for the efficient removal of persistent organic contaminants from municipal wastewater. By addressing both technical and sustainability challenges,

PMR technology can play a pivotal role in advancing water reuse and supporting future circular water management strategies.

## Author contributions

Veronica Cozzolino: writing – original draft, investigation, data curation. Gerardo Coppola: writing – original draft, methodology. Sudip Chakraborty: conceptualization, writing – writing – review & editing. Giovanni Chiappetta: investigation, writing – review & editing. Alessio Siciliano: conceptualization, writing – review & editing. Carlo Limonti: writing – review & editing. Giulia Maria Curcio: writing – review & editing. Catia Algieri: writing – review & editing, investigation, data curation, conceptualization. Vincenza Calabrò: conceptualization, writing – review & editing, resources.

## Conflicts of interest

There are no conflicts to declare.

## Data availability

The data that support the findings of this study are available from the corresponding author, Dr Catia Algieri, upon request.

## Acknowledgements

This work has received funding from MIUR-PNRR: “Tech4You - Technologies for climate change adaptation and quality of life improvement”, codice identificativo ECS 00000009, Spoke 2, Pilot 2.2.1.

## References

- 1 P. G. Wells, *Mar. Pollut. Bull.*, 2013, **69**, 1–2.
- 2 N. Abd Rahman, C. E. Choong, S. Pichiah, I. W. Nah, J. R. Kim, S. E. Oh, Y. Yoon, E. H. Choi and M. Jang, *Sep. Purif. Technol.*, 2023, **304**, 122294.
- 3 T. D. Kusworo, B. Budiyo, A. C. Kumoro and D. P. Utomo, *J. Environ. Manage.*, 2022, **317**, 115357.
- 4 Y. Jin and A. Davarpanah, *Water, Air, Soil Pollut.*, 2020, **231**, 441.
- 5 E. E. Mitsika, C. Christophoridis, N. Kouinoglou, N. Lazaridis, C. K. Zacharis and K. Fytianos, *J. Hazard. Mater.*, 2021, **403**, 123819.
- 6 A. J. A. Simões, R. O. Macêdo-Júnior, B. L. P. Santos, D. P. Silva and D. S. Ruzene, *Water, Air, Soil Pollut.*, 2021, **232**, 297.
- 7 Ö. Gökkuş, E. Brillas and I. Sirés, *Sci. Total Environ.*, 2024, **912**, 169143.
- 8 F. Çiner and Ö. Gökkuş, *Clean: Soil, Air, Water*, 2013, **41**, 80–85.
- 9 O. Samuel, M. H. D. Othman, R. Kamaludin, H. Dzinun, A. Imtiaz, T. Li, T. El-badawy, A. U. Khan, M. H. Puteh, E.



- Yuliwati, T. A. Kurniawan and M. T. Moreira, *J. Cleaner Prod.*, 2023, **415**, 137567.
- 10 P. Swaminaathan, A. Saravanan, P. R. Yaashikaa and A. S. Vickram, *Sustain. Chem. Environ.*, 2024, **8**, 100171.
  - 11 C.-J. Wu, I. V. Maggay, C.-H. Chiang, W. Chen, Y. Chang, C. Hu and A. Venault, *Chem. Eng. J.*, 2023, **451**, 138990.
  - 12 R. Janssens, R. Hainaut, J. Gillard, H. Dailly and P. Luis, *Ind. Eng. Chem. Res.*, 2021, **60**, 2223–2231.
  - 13 S. Bhattacharyya, C. Algieri, M. Davoli, V. Calabrò and S. Chakraborty, *Chem. Eng. Res. Des.*, 2023, **193**, 641–648.
  - 14 A. Yuan and J. Toweh, *Open J. Polit. Sci.*, 2025, **15**, 510–531.
  - 15 R. J. Mathar, *J. Opt. A: Pure Appl. Opt.*, 2007, **9**, 470.
  - 16 A. F. Caliman, C. Cojocaru, A. Antoniadis and I. Poullos, *J. Hazard. Mater.*, 2007, **144**, 265–273.
  - 17 E. Bizani, D. Lambropoulou, K. Fytianos and I. Poullos, *Environ. Sci. Pollut. Res.*, 2014, **21**, 12294–12304.
  - 18 E. Bizani, K. Fytianos, I. Poullos and V. Tsiroidis, *J. Hazard. Mater.*, 2006, **136**, 85–94.
  - 19 S. Riaz and S. J. Park, *J. Ind. Eng. Chem.*, 2020, **84**, 23–41.
  - 20 R. Molinari, C. Lavorato and P. Argurio, *Catalysts*, 2021, **11**, 775.
  - 21 M. Salaices, B. Serrano and H. I. De Lasa, *Chem. Eng. J.*, 2002, **90**, 219–229.
  - 22 M. Litter, P. Boule, D. Bahnemann and P. Robertson, *Environ. Photochem. Pt. II*, 2005, **2**, 400–490.
  - 23 R. Molinari, C. Lavorato and P. Argurio, *Catalysts*, 2020, **10**, 1–38.
  - 24 A. Bhattacharya and S. Ambika, *Progression and Application of Photocatalytic Membrane Reactor for Dye Removal: An Overview*, Springer Singapore, 2022.
  - 25 S. Bhattacharyya, L. Donato, S. Chakraborty, V. Calabrò, M. Davoli and C. Algieri, *Earth Syst. Environ.*, 2025, **9**, 639–652.
  - 26 N. Liu, Z. Sun, H. Zhang, L. H. Klausen, R. Moonhee and S. Kang, *Sci. Total Environ.*, 2023, **875**, 162603.
  - 27 I. S. Thakur and K. Medhi, *Bioresour. Technol.*, 2019, **282**, 502–513.
  - 28 M. A. Syed, A. K. Mauriya and F. Shaik, *Int. J. Environ. Anal. Chem.*, 2022, **102**, 4518–4534.
  - 29 K. Y. Pete, J. Kabuba, B. Otieno and A. Ochieng, *Environ. Sci. Pollut. Res.*, 2023, **30**, 94154–94165.
  - 30 M. Binazadeh, J. Rasouli, S. Sabbaghi, S. M. Mousavi, S. A. Hashemi and C. W. Lai, *Materials*, 2023, **16**, 2522–2565.
  - 31 S. Bhattacharyya, C. Algieri, M. Davoli, V. Calabrò and S. Chakraborty, *Chem. Eng. Res. Des.*, 2023, **193**, 641–648.
  - 32 J. F. Blanco, J. Sublet, Q. T. Nguyen and P. Schaetzel, *J. Membr. Sci.*, 2006, **283**, 27–37.
  - 33 M. B. Asif and Z. Zhang, *Chem. Eng. J.*, 2021, **418**, 129481.
  - 34 E. K. Tetteh, S. Rathilal and D. B. Naidoo, *Sci. Rep.*, 2020, **10**, 1–12.
  - 35 W. Z. Khan, *IOSR-JEN*, 2016, **06**, 36–46.
  - 36 C. Munien, E. Kweinor Tetteh, T. Govender, S. Jairajh, L. L. Mguni and S. Rathilal, *Appl. Sci.*, 2023, **13**, 4766.
  - 37 N. S. Topare, M. Joy, R. R. Joshi, P. B. Jadhav and L. K. Kshirsagar, *J. Indian Chem. Soc.*, 2015, **92**, 219–222.
  - 38 M. N. Chong, Y. J. Cho, P. E. Poh and B. Jin, *J. Cleaner Prod.*, 2015, **89**, 196–202.
  - 39 C. P. M. de Oliveira, M. M. Viana, G. R. Silva, L. S. Frade Lima, E. Coutinho de Paula and M. C. S. Amaral, *J. Cleaner Prod.*, 2020, **257**, 120526.
  - 40 M. Xu, Y. Gao, E. M. Moreno, M. Kunst, M. Muhler, Y. Wang, H. Idriss and C. Wöll, *Phys. Rev. Lett.*, 2011, **106**, 1–4.

